

## Imaging Borrelly

L.A. Soderblom,<sup>a,\*</sup> D.C. Boice,<sup>b</sup> D.T. Britt,<sup>c</sup> R.H. Brown,<sup>d</sup> B.J. Buratti,<sup>e</sup> R.L. Kirk,<sup>a</sup> M. Lee,<sup>e</sup> R.M. Nelson,<sup>e</sup> J. Oberst,<sup>f</sup> B.R. Sandel,<sup>g</sup> S.A. Stern,<sup>h</sup> N. Thomas,<sup>i</sup> and R.V. Yelle<sup>d</sup>

<sup>a</sup> *United States Geological Survey, 2255 N Gemini Drive, Flagstaff, AZ 86001, USA*

<sup>b</sup> *Southwest Research Institute, Space Sciences and Engineering Division, 6220 Culebra Road, PO Drawer 28510, San Antonio, TX 78228-0510, USA*

<sup>c</sup> *Department of Physics, The University of Central Florida, PO Box 162385, Orlando, FL 32816-2385, USA*

<sup>d</sup> *Departments of Planetary Sciences and Astronomy, University of Arizona, 1629 E. University Boulevard, Tucson, AZ 85721, USA*

<sup>e</sup> *Jet Propulsion Laboratory, California Institute of Technology, 4800 Oak Grove Drive, Pasadena, CA 91109, USA*

<sup>f</sup> *German Aerospace Center, Institute of Planetary Research, Rutherfordstrasse 2, D-12489 Berlin, Germany*

<sup>g</sup> *Lunar and Planetary Laboratory, 1040 East Fourth Street, Room 901, University of Arizona, Tucson, AZ 85721, USA*

<sup>h</sup> *Department of Space Studies, Southwest Research Institute, 1050 Walnut St., Suite 400, Boulder, CO 80302, USA*

<sup>i</sup> *Space Research and Planetology Division, Physikalisches Institut, Sidlerstr. 5, CH-3012 Bern, Switzerland*

Received 25 November 2002; revised 6 June 2003

### Abstract

The nucleus, coma, and dust jets of short-period Comet 19P/Borrelly were imaged from the Deep Space 1 spacecraft during its close flyby in September 2001. A prominent jet dominated the near-nucleus coma and emanated roughly normal to the long axis of nucleus from a broad central cavity. We show it to have remained fixed in position for more than 34 hr, much longer than the 26-hr rotation period. This confirms earlier suggestions that it is co-aligned with the rotation axis. From a combination of fitting the nucleus light curve from approach images and the nucleus' orientation from stereo images at encounter, we conclude that the sense of rotation is right-handed around the main jet vector. The inferred rotation pole is approximately perpendicular to the long axis of the nucleus, consistent with a simple rotational state. Lacking an existing IAU comet-specific convention but applying a convention provisionally adopted for asteroids, we label this the north pole. This places the sub-solar latitude at  $\sim 60^\circ$  N at the time of the perihelion with the north pole in constant sunlight and thus receiving maximum average insolation.

© 2003 Elsevier Inc. All rights reserved.

*Keywords:* Comet; Imaging; Nucleus; Topography; Coma; Dust jet; Short-period comets; 19P/Borrelly; Borrelly; Deep Space 1; Rotation axis; Rotation pole

### 1. Introduction

At the completion of its mission, the ion propulsion-powered NASA Deep Space 1 (DS1) spacecraft achieved a close encounter with 19P/Borrelly, a Jupiter-family short-period comet. Developed under NASA's New Millennium Program by the Jet Propulsion Laboratory, DS1 is the first ion-propulsion spacecraft ever flown in deep space (see Rayman 2001, 2002; Rayman and Varghese, 2001; Nelson and Rayman, this issue, for summaries). The encounter occurred at 22:29:33 UTC on September 22, 2001 DS1 passed  $2171 \pm 10$  km from the comet's nucleus on the sunward side at a relative speed of 16.58 km/s. The encounter occurred at

a heliocentric range of 1.36 AU only 8 days after the comet's perihelion passage.

Comets 1P/Halley and 19P/Borrelly are now the only comets whose nuclei have been imaged close-up by spacecraft (Keller et al., 1987; Soderblom et al., 2002). Halley is an intermediate period comet that is believed to be compositionally representative of distant long-period comets in the Oort cloud. Borrelly is a short-period Jupiter-family comet the source region for which is thought to be the Kuiper belt. The Borrelly observations discussed in this issue then represent our first view of a Jupiter-family comet nucleus and significantly broaden our understanding of cometary nuclei.

From observations of Borrelly with the Hubble Space Telescope during the 1994 apparition, Lamy et al. (1998) derived a rotation period of  $25 \pm 0.5$  hours and, assuming an albedo of 0.04, an elongate shape with a semi-major axis  $4.4 \pm 0.3$  km and semi-minor axis  $1.8 \pm 0.15$  km. DS1 obser-

\* Corresponding author.

E-mail address: [isoderblom@usgs.gov](mailto:isoderblom@usgs.gov) (L.A. Soderblom).

Table 1  
Summary of MICAS characteristics

	UV imaging spectrometer	APS imager	VISCCD imager	SWIR image spectrometer
Detector type	1024 × 2048 FT CCD	JPL APS 256 <sup>2</sup>	1024 × 2048 FT CCD	Rockwell PICNIC
Wavelength range (nm)	80–185	500–1000	500–1000	1200–2400
Aperture diameter (mm)	100	100	100	100
Effective focal length (mm)	171	677	677	752
F/number	1.7	6.8	6.8	7.5
Detector array size	35 × 164	256 × 256	1024 × 1024	256 × 256
Pixel size (microns)	54	12	9	40
FOV (deg)	0.63 × 0.03	0.26 × 0.26	0.69 × 0.78	0.7 × 0.003
IFOV (microrad/pixel)	316	17.9	13.4	54
Spectral sampling interval	0.64	n/a	n/a	6.6
Spectral resolution (nm)	2.1	n/a	n/a <td 12	

vations showed these early estimates of the properties of the nucleus by Lamy and colleagues were remarkably accurate; Soderblom et al. (2002) reported an elongate nucleus with a long axis of 8 km and geometric albedo of  $0.03 \pm 0.005$ .

The DS1 spacecraft carried an advanced technology integrated remote sensing instrument, MICAS (Miniature Integrated Camera and Spectrometer, Soderblom et al., 2000), the characteristics of which are shown in Table 1; the optical layout is shown in a companion article (Soderblom et al., this issue). Of the four MICAS channels only the VISCCD Imager (Visible-light Charge Coupled Device) and SWIR Imaging Spectrometer (Short-Wavelength Infrared) returned useful scientific data from the Borrelly encounter. The detector for the UV Imaging Spectrometer failed soon after launch; the APS (Active Pixel Sensor) Imager had been set up for use on bright targets (Earth, Moon, Mars, Jupiter) so it was too insensitive to record the dim light levels of Borrelly's coma, jets, and surface. The results from the SWIR imaging spectrometer are described in a separate article (Soderblom et al., this issue).

Borrelly currently has an orbital period of 6.86 years, a perihelion distance of 1.358 AU, and an orbital inclination of  $30.3^\circ$  (IAU MPC 31664, 1998). At encounter, the DS1 spacecraft was close to the plane of the ecliptic and ahead of the Earth  $\sim 75^\circ$  in terms of orbital longitude. During the DS1 approach, the view of the comet was in the direction of ecliptic south as it rose in its inclined orbit toward the spacecraft (Fig. 1). During the last  $\sim 90$  minutes before closest approach when the nucleus and details of the coma and dust jets were resolved, 52 visible-wavelength images were collected with the MICAS VISCCD camera. Closest approach was chosen to be on the sunward side of the nucleus; this provided optimum phase angles for viewing the surface of the nucleus, minimizing stray sunlight in the optics that became increasingly significant when the MICAS bore sight was closer than  $\sim 90^\circ$  to the Sun. The images cover solar phase angles from  $88^\circ$  to  $52^\circ$  and provide stereoscopic coverage of the coma, jets, and nucleus. Soderblom et al. (2002) reported initial Borrelly encounter results from MICAS; the present article describes in much greater detail the data set, image processing, and the analysis of images made by the MICAS VISCCD camera and sets the stage other articles

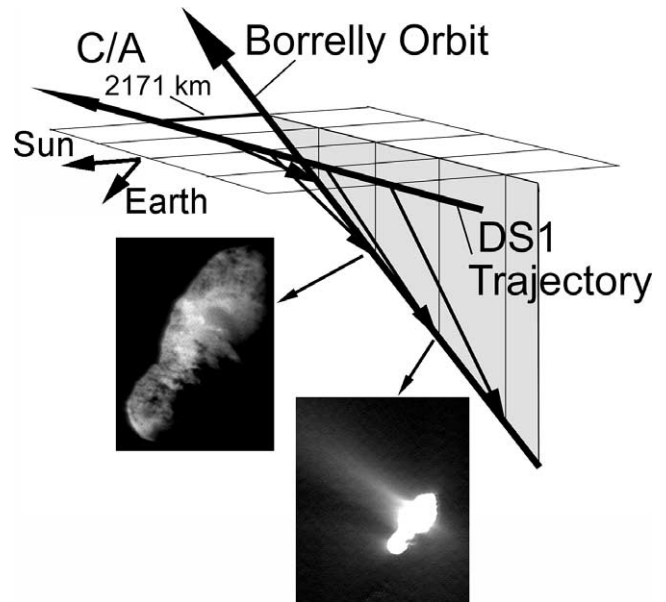


Fig. 1. DS1-Borrelly encounter geometry. The DS1 trajectory was nearly in the plane of the ecliptic (horizontal plane). Borrelly was imaged as rose in its inclined orbit from ecliptic south toward the spacecraft. Two images are shown in schematic position: the best image of the nucleus (CCD\_NEAR\_1, upper) and the best of the dust jets (CCD\_MID\_5\_2, lower).

contained in this issue. *Note that for all images of the comet shown in this article, the sunlight comes from the left of the frame.*

## 2. Imaging instrumentation, data set, and processing

The near encounter imaging sequence commenced at about  $-87$  minutes. Table 2 provides detail for the full-frame images that were collected during this phase. The raw and processed image data and SPICE (Spacecraft-Target Body Geometry, Pointing Matricies, Event Files) are available on line at [http://astrogeology.usgs.gov/Projects/DeepSpace1/MICAS\\_Archive/index.htm](http://astrogeology.usgs.gov/Projects/DeepSpace1/MICAS_Archive/index.htm).

Additional sub-frames were collected and stored by the onboard autonomous tracking S/W (see Bhaskaran et al.,

Table 2  
Near encounter images characteristics and quality

MICAS VISCCD image name	Time relative to C/A (s)	Phase angle	Exposure (msec)	Range (km)	Resolution (m/pixel)	Degree of nucleus blur	Comments on use of image for nucleus, jet, and/or coma photometry
CCD_RSEN_1	-5236	87.7	874	86861.2	1141.4	Minor	No scratch interference
CCD_FAR_1_4	-4996	87.6	874	82882.2	1089.1	Minor	No scratch interference
CCD_FAR_1_5	-4966	87.6	1750	82384.9	1082.5	Minor	No scratch interference
CCD_SRSEN_3	-1856	85.1	154	30854.6	405.4	Good sharp nucleus	No scratch interference
CCD_SRSEN_20	-1346	83.6	307	22425.3	294.7	Good sharp nucleus	No scratch interference
CCD_BORE_13	-781	79.6	307	13130.5	172.5	Good sharp nucleus	No scratch interference
MID_1_1	-578	76.4	614	9825.9	129.1	Severe	Top coma clear; main jet cut off at bottom
MID_1_2	-548	75.7	109	9341.3	122.7	Minor	No scratch interference
MID_2_1	-518	75.0	218	8858.2	116.4	Minor	Nucleus barely clear; crab on main jet
MID_2_2	-483	74.0	109	8296.6	109.0	Minor	No scratch interference
MID_3_1	-437	72.5	218	7562.7	99.4	Moderate	Crab on nucleus; main jet clear; L–R scattering
MID_3_2	-407	71.3	614	7087.8	93.1	Moderate	Crab on upper nucleus; main jet clear
MID_4_1	-377	70.0	109	6616.0	86.9	Severe	Weak crab part on nucleus; jet clear
MID_4_2	-347	68.5	218	6148.2	80.8	Severe	Weak crab part on nucleus; jet clear
MID_5_1	-290	64.9	109	5274.3	69.3	Severe	No scratch interference
MID_5_2	-260	62.5	218	4825.3	63.4	Minor	No scratch interference
MID_5_3	-230	59.6	77	4386.7	57.6	Good sharp nucleus	Exclamation on small end nucleus; jet clear
MID_5_4	-200	56.0	154	3962.0	52.1	Minor w/strong linear smear	Exclamation on nucleus; jet clear
NEAR_1	-170	51.6	77	3556.3	46.7	Minor w/mild linear smear	Exclamation near main jet first 6 km

2002). These frames (termed “snips”) contain only  $100 \times 100$  pixels (of the  $1024 \times 1024$  full frame). Although most contain all or part of the nucleus, all are very low in resolution and because, they are incomplete, they cannot be properly corrected to radiance units. They are not included in the scientific data set.

MICAS is a derivative of PICS (Pluto Integrated Camera Spectrometer; Beauchamp et al., 1994). The key new technology is the monolithic silicon carbide (SiC) construction used for the integrated structure, optical bench, and optics. This material was essential to realize the very low mass and to achieve combined thermal and optical stability requirements. It allows a design that can be assembled at room temperature and will stay aligned and in focus when cooled to cryogenic operating temperatures. It also makes optical alignment immune to thermal gradients across an instrument with several focal planes held at different temperatures. Thermal stability of the PICS/MICAS optical design was solidly demonstrated in thermal vacuum tests. Systems were aligned at room temperature and cycled to cryogenic operating temperatures exhibiting negligible change in alignment; interferometric measurement showed optical stability down to a precision of  $1/10$  wave (Beauchamp et al., 1994).

The MICAS VISCCD camera used a  $1024 \times 2048$  CCD with  $9\text{-}\mu\text{m}$  pixels operated in a continuous frame-transfer mode. The detector array was continuously clocked down-column at  $\sim 6 \mu\text{sec}/\text{line}$  so that transfer of the  $1024 \times 1024$  active imaging area into the masked area required  $\sim 6$  msec. Because the detector was maintained between 140 and 160 K, dark current buildup was miniscule, even for the longer, several-second exposures. At Borrelly, the bias level background was extremely flat and constant at  $\sim 140$  DN. A weak down-column streaking arises from continuous transfer of charge from a bright target down the



Fig. 2. Raw VISCCD image (CCD\_MID\_5\_2).

image that builds up in the serial register. For study of the nucleus this streaking is negligible but in the case of faint signals of the dust coma and jets this effect is quite apparent. Figure 2 shows this effect in a raw image that has been stretched to show faint coma and saturate the much brighter nucleus. The vertical streaks were removed by averaging sections of lines free of coma and/or nucleus and subtracting this average from each line. Residuals from the vertical streaks are typically  $< 1\%$  of the coma brightness and are less than the residual coherent noise.

The raw VISCCD is non-linear near the “toe” of the light transfer curve (LTC). Within the first  $\sim 100$  DN

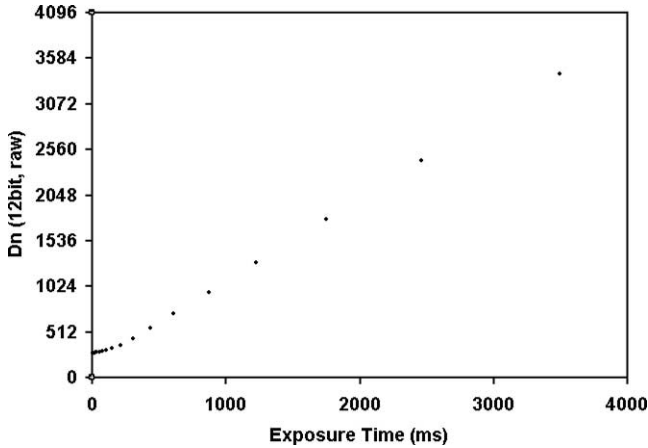


Fig. 3. VISCCD light transfer laboratory data showing strong non-linear behavior at low light levels. This characteristic is uniform over the detector field and was validated with in-flight calibration observations.

above the dark level bias, the LTC exhibits lower sensitivity (DN/photon); over the remaining range (100-4096 DN) the LTC is quite linear. Figure 3 shows a set of laboratory data used to derive a correction for this characteristic. This characteristic is uniform over the detector field and was validated with in-flight calibration observations using stray sunlight as the calibration source. The LTC non-linearity is quite uniform over the field and a single function was used to “linearize” all pixel

The next step in radiometric calibration is conversion to an absolute radiometric scale expressed in terms of a radiance factor,  $I/F$ . For a Lambertian target viewed and illuminated normal to its surface  $I/F = 1$  (i.e.,  $i = 0$  and  $\varepsilon = 0$ ). This factor is conceptually simple; it is a dimensionless quantity akin to albedo and is in fact equal to normal albedo for  $i = 0$  and  $\varepsilon = 0$ . The correction factor to reduce the linearized DN above the background to  $I/F$  is defined as  $\omega_0$ , a calibration parameter defined as the expected brightness in DN/s of a Lambertian target located at 1 AU from the Sun that is illuminated and imaged normal to its surface. The radiance factor  $I/F$  can be converted to absolute flux by simply multiplying by the solar radiance at the target distance. Using VISCCD images of Mars acquired from DS1 during November 1999, we estimate  $\omega_0 \sim 2.9 \times 10^6$  DN/s. This value is uncertain by  $\sim 20\%$ , assigned principally from uncertainty in photometric modeling the expected  $I/F$  for Mars. This compares reasonably well with the original design value for  $\omega_0$  of  $4 \times 10^6$  DN/s. The full equation used to convert raw DN to  $I/F$  is of the form  $[Ax + B + C/(x + D)] \times R_{\odot}^2 / (\omega_0 \times \text{EXP})$ , where  $x$  is raw DN above the bias. The full expression is:

$$I/F = [0.95 \times (\text{DN}_{\text{raw}} - \text{DC}_{\text{bias}}) + 122.0 \\ - 4.63 \times 10^{-20} / (\text{DN}_{\text{raw}} - \text{DC}_{\text{bias}} + 300.0)] \\ \times R_{\odot}^2 / (2.9 \times 10^6 \times \text{EXP}),$$

where  $\text{DN}_{\text{raw}}$  is raw data number,  $\text{DC}_{\text{bias}}$  is the constant dark offset bias ( $\sim 140$  DN for Borrelly),  $R_{\odot}$  is the heliocentric

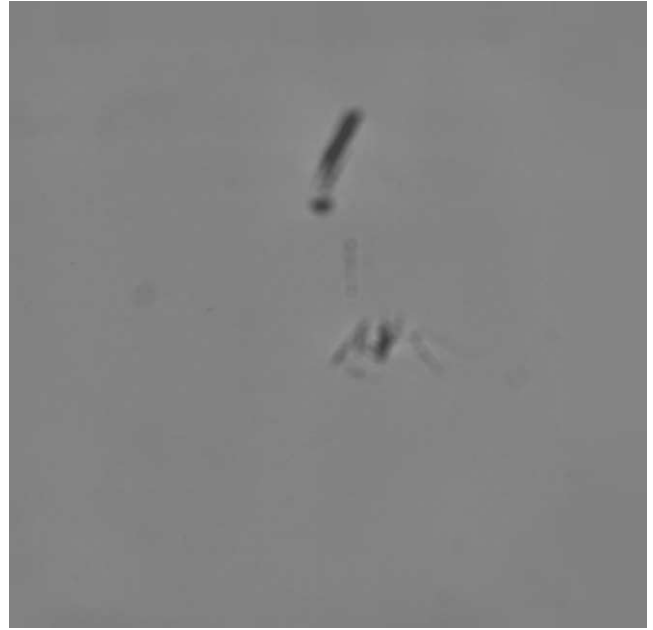


Fig. 4. Field-of-view shading variations in the VISCCD response. These features arose from two clusters of scratches on the MICAS primary. They are nicknamed the “exclamation” (upper feature) and the “crab” (lower feature) for reference in Table 2.

range to the target in AU and EXP is the VISCCD exposure time in seconds.

The next step is to remove shading variations across the FOV. In general, the shading across the field is negligible, owing to the narrow-field optics and the uniform response across the detector. Unfortunately in-flight flat-field calibration frames could not be acquired owing to severe stray light contamination when the S/C was turned so that the calibration target was illuminated. Some flat fields were acquired in the laboratory but variability of the flat-field illumination was of order 10%, much larger than expected sensitivity variations across the FOV. As a consequence we have assumed the overall sensitivity across the field to be constant. However these laboratory flat fields were found invaluable to correct for high-frequency variations in the field shading. Because of last minute schedule and cost constraints some scratches had to be left on the primary mirror. Figure 4 shows two clusters of blemishes introduced in the VISCCD field as a result. They are nicknamed (upper feature the “exclamation” and lower feature the “crab”) for reference in Table 2. For the most part they introduce modulations in shading field and are largely removed by division in the calibration procedure. However another manifestation of them that is more difficult, if not impossible to remove, is introduced when the nucleus falls on one of the scratch clusters. In this situation the scratches scatter light from the nucleus image into the nearby and much fainter coma and jets in the image. The best course is to avoid such images in analysis of the coma features; these “contaminated” images are noted in Table 2.

Another step in the processing was to suppress a low-level quasi-coherent noise pattern from the images; this pattern

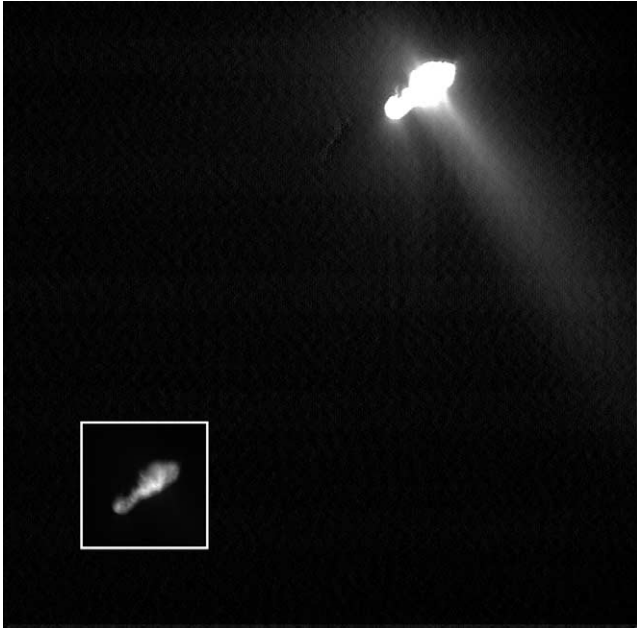


Fig. 5. VISCCD image after radiometric corrections and coherent noise suppression (same image as in Fig. 2). Small inset is stretched to show the nucleus demonstrating the large dynamic range in the images.

is visible in Fig. 2 as a series of short horizontal streaks. This pattern is at such low level that it has little effect on the nucleus images and its removal is unnecessary for nucleus study. However, it is clearly evident if the images are stretched to study the coma. This pattern was suppressed by spatial filtering (the sum of a pair of high-pass and low-pass boxcar filters tuned to the wavelength of the pattern). The final product of the radiometric-cosmetic processing is illustrated in Fig. 5.

Smear or image blur was generally quite low but as the turn rate to dynamically track the target increased toward C/A, the mismatch in rate also increased. A final step, optionally applied to several of the high-resolution images of the nucleus, was deblurring. In the CCD images, two types of blurring are present at some level: optical blurring and motion blurring. A maximum likelihood algorithm was employed with a blurring kernel tailored for each image (Lee et al., 2002). The blurring kernel was created by interactively constructing a two-dimensional motion template and convolving it with the point spread function of MICAS VISCCD channel. In some cases the blurring motion was quite variable requiring a complex motion template. Between 20 and 40 iterations were required, depending on the severity of the blur. Figure 6 shows the effect of blur removal for the highest resolution image of the nucleus (CCD\_NEAR\_1). These versions were useful for stereogrammetric mapping of the nucleus (cf. Kirk et al. and Oberst et al., this issue). Table 2 provides comments on the quality of the scientifically useful 19 near-encounter images in terms of scattering by the scratches contaminating the coma and degree of smear of images for nucleus studies.

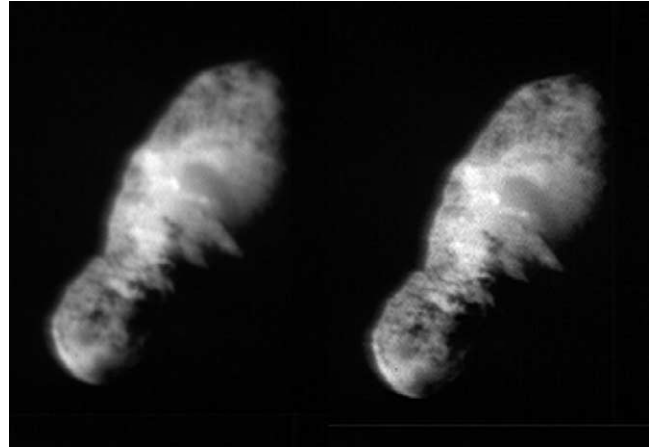


Fig. 6. Deblurring applied to remove a small degree of image-motion blur in the highest-resolution image (CCD\_NEAR\_1).

### 3. Near-nucleus geometric structure of Borrelly's coma

During the 14 apparitions that it has been observed during the  $\sim 100$  years since its discovery, Borrelly has historically exhibited a strong sunward asymmetry in its coma. This manifests itself as an elongation of the coma toward the sun. Ground-based telescopes and Hubble Space Telescope images reveal this elongation to be a narrow beam extending out for thousands of kilometers (cf. Lamy et al., 1998; Samarasinha and Mueller, 2002; Farnham and Cochran, 2002; Schleicher et al., 2003; Weaver et al., 2003).

In early DS1 approach images this sunward asymmetry was resolved into two separate components. Figure 7 is a composite of 5 images acquired during the last navigation approach image sequence at  $-10.4$  hr (Table 3) and is transitional in scale between the Earth-based images and the DS1 near encounter images. This was a particularly good observation; the S/C was extremely steady (owing to use of the ion propulsion system for attitude control) and the comet was captured in a part of the frame free of complex patterns from



Fig. 7. Composite image from final approach image set acquired 10.4 hr before encounter at a range of 0.62 million km. The image on the right has had a log stretch applied. The fan jet is sun-pointed (Sun to left); the main jet is canted  $\sim 35^\circ$  clockwise from the sun line. These two jets remained fixed in orientation for at least a full rotation period.

Table 3  
Approach image observations of Borrelly

Observation name	Time relative to C/A (hr)	UTC date	Phase angle	Borrelly-DS1 range (km)	Borrelly-Sun range (AU)
SOB01	-686.1	8/25/01	75.2	4.03E+07	1.3788
SOB02	-589.9	8/29/01	77.1	3.48E+07	1.3715
SOB03	-366.0	9/7/01	81.6	2.17E+07	1.3607
SOB04	-300.9	9/10/01	82.9	1.79E+07	1.3591
SOB05	-221.9	9/13/01	84.6	1.32E+07	1.3583
SOB06	-182.5	9/15/01	85.4	1.09E+07	1.3582
SOB07	-153.0	9/16/01	86.0	9.13E+06	1.3584
SOB08	-111.2	9/18/01	86.8	6.63E+06	1.3588
SOB09	-54.2	9/20/01	88.0	3.23E+06	1.3600
SOB010	-34.4	9/21/01	88.4	2.05E+06	1.3605
SOB011	-10.4	9/22/01	88.7	6.21E+05	1.3612

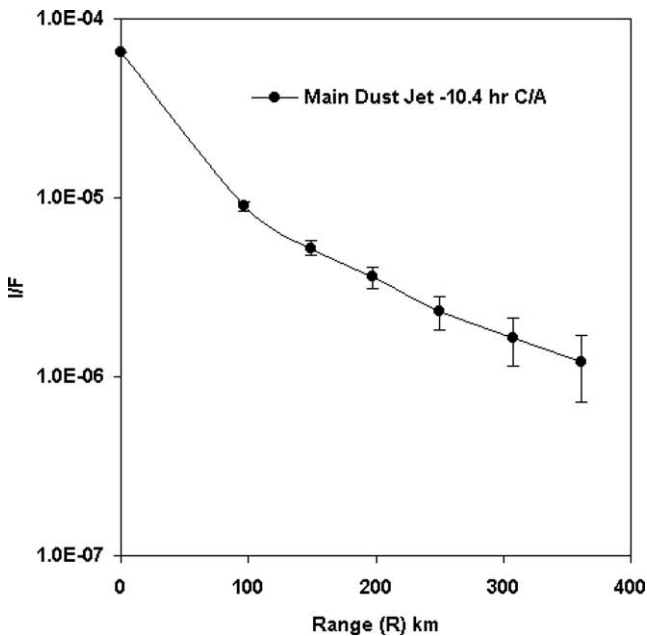


Fig. 8. Photometric profile along length of the main jet shown in Fig. 7. The main jet is detectable out to  $> 400$  km where it falls below the VISCCD detection limit:  $I/F \sim 10^{-6}$ .

scattered stray light. As a result two discrete dust jets can be seen extending for roughly 400 km from the nucleus out to a limit in  $I/F \sim 10^{-6}$  (Fig. 8). One jet is sun-pointed (termed “fan jet”); the other, somewhat more pronounced (termed “main jet”), is canted roughly  $30^\circ$  forward (in a prograde sense) from the Sun (which is to the left and near the plane of the image, phase angle  $\sim 88^\circ$ ). These two jets dominated the inner coma and remained fixed in inertial orientation for the rest of the encounter over which the nucleus rotated an additional  $\sim 140^\circ$ . We conclude that the main jet is aligned with the rotation axis and remains fixed in orientation; while the fan jet tracks the Sun as the object rotates generating a moving fan at the sub-solar point.

Whereas the fan jet remained diffuse in appearance as resolution increased, the main jet resolved into highly collimated components (Soderblom et al., 2002). The fan jet is centered on the sun-line and at near encounter emanated from an extended source area across the small, smooth end of the nucleus. In Fig. 9 two of the best MICAS images of the near-nucleus coma have been enhanced to show details of the dust jets. The expanding, fan-shaped jet represents the simple case that one would expect to see from dust entrained in a plume of gas expanding from a small region of subliming ice exposed at the surface. It is noteworthy that its intensity changed substantially: relative to the main jet, the fan jet is much more prominent at  $-10.4$  hr in Fig. 7 than it is at  $-4$  min in Fig. 9. Presumably this modulation arises as the sub-solar point moves across the nucleus across areas more or less volatile rich. The small end, sun-pointed at encounter, was evidently far less prolific than the region that was sun-pointed at the time of SOB11 (roughly the opposite hemisphere).

The main jet consists of series of collimated jets with different directions. The left image (A) in Fig. 9 shows a highly collimated jet that is at the core of the main jet; this was termed by Soderblom et al. (2002) as the  $\alpha$  jet. The right image (B) shows a view in which a series of smaller collimated jets, visibly extending out to about 5 km from the nucleus, are superposed on the  $\alpha$  jet and differ in direction from it.

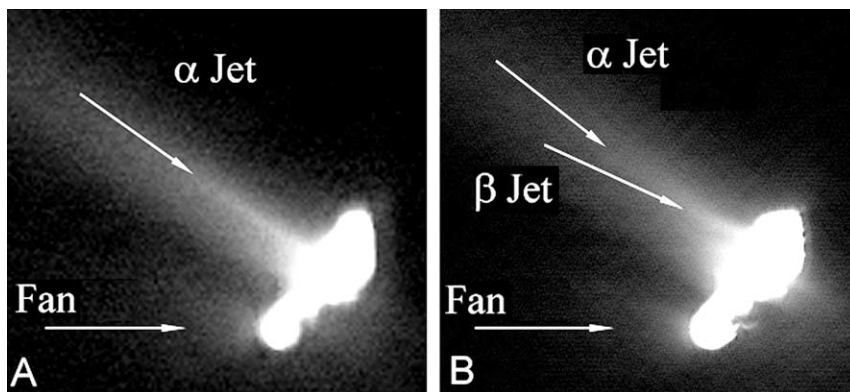


Fig. 9. Two high-resolution images (173 and 63 m/pixel) showing details in the near-nucleus coma and dust jet features: (A) image CCD\_BORE\_13; (B) image CCD\_MID\_5\_2 (see Table 2 for image parameters).

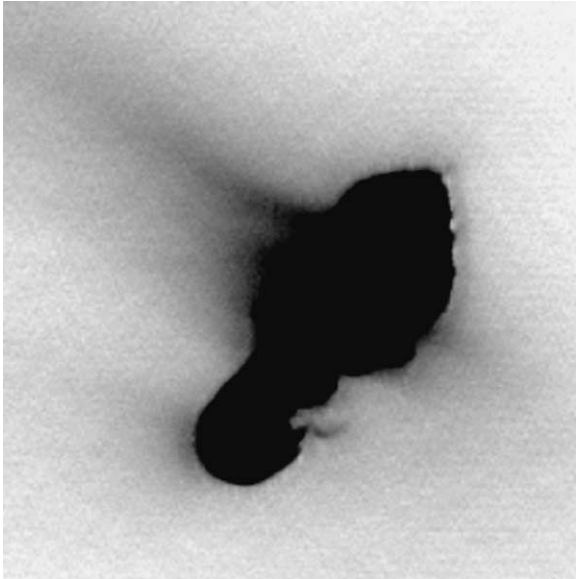


Fig. 10. Image B in Fig. 9 is shown inverted with a stretch to enhance the apparent curvature along the upper margin of the jet. This curvature arises from the superposition of the  $\alpha$  and  $\beta$  jets in this perspective.

The principal one of these secondary jets is referred to as the  $\beta$  jet (Soderblom et al., 2002).

This best way to familiarize oneself with the complex structure of the main jet is through viewing movies of the 7 best jet images (these are available at <http://astrogeology.usgs.gov/Projects/DeepSpace1>). In individual images distinguishing the  $\alpha$  and  $\beta$  jets is more difficult but there are several visual clues:

- (a) in the simplest case two sets of jets appear superposed as just described (Fig. 9B);
- (b) often the isophotes at the margin of the jet appear to curve or turn as one jet emerges behind another (Fig. 10);
- (c) in the earlier images the isophotes appear to converge—coming to a triangular point—as two jets cross one another and add in brightness.

Using such features and studying the movies in great detail, we have attempted to map the  $\alpha$  and  $\beta$  jets; this process is somewhat subjective and not all together satisfying. Figures 11 and 12 illustrate the results for five of the best near-encounter frames. Figure 12 is shown in two contrast stretches: one to show the jets and a second to show the surface patterns where the jet traces intersect. As noted by Soderblom et al. (2002) there is a suggestion that the  $\beta$  jet originates in a dark oval spot just inside the limb of the nucleus most visible in the last two frames. Owing to the uncertainty in distinguishing the individual jets, it is also reasonable that this jet originates farther toward the central brighter region. Because of the parallel nature of the traces along the  $\alpha$  jet, its source location is even more ambiguous. However the trace along the narrow sharp jet at its core, best

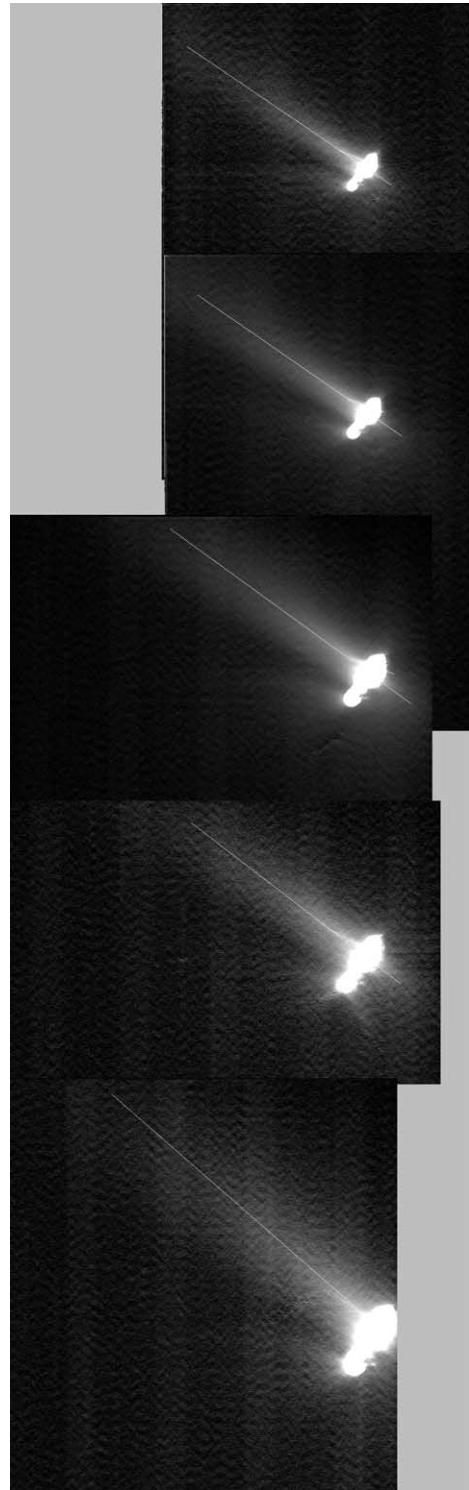


Fig. 11. Time sequence showing traces of the  $\alpha$  jet as its angular direction in the images changed during the flyby. The images from top to bottom are: CCD\_MID\_4\_1, CCD\_MID\_4\_2, CCD\_MID\_5\_2, CCD\_MID\_5\_3, and CCD\_NEAR\_1 (see Table 2 for parameters).

distinguished in the earlier frames (Fig. 9A), coincidentally traces across the brightest region in the central part of the nucleus near the location of the inferred rotation pole that is discussed below.

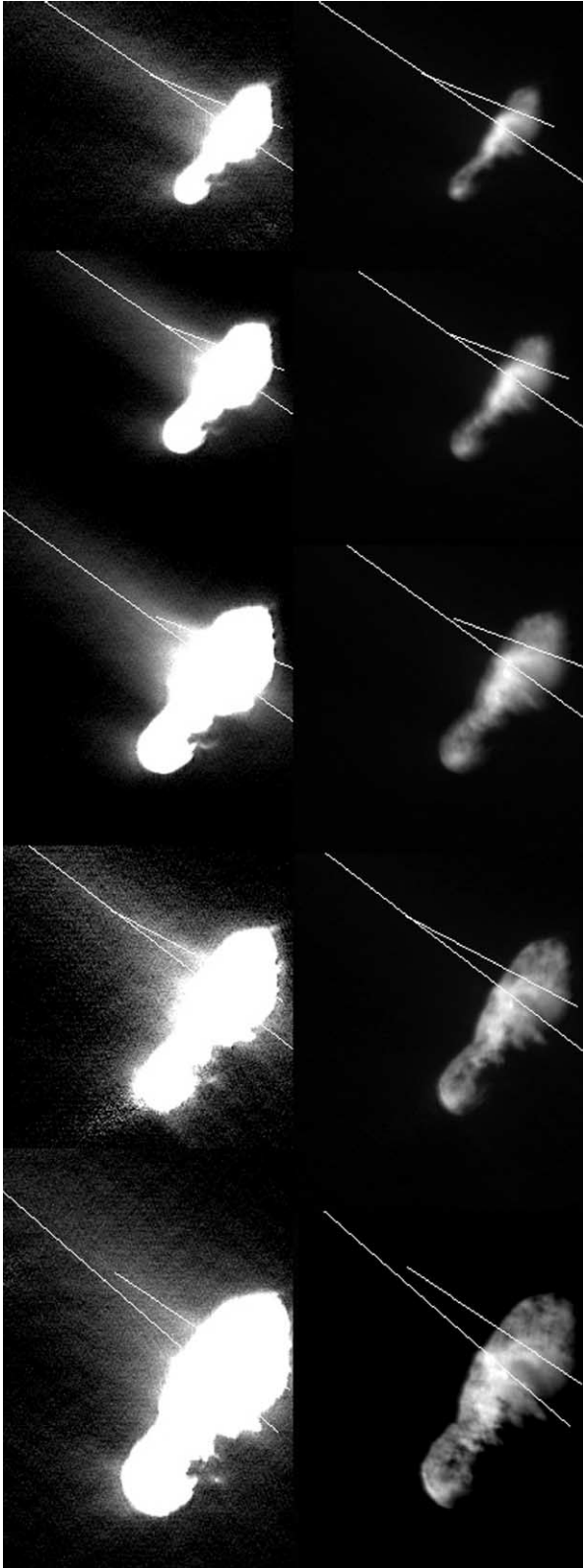


Fig. 12. Enlargement of the image time sequence of Fig. 11 to show the traces of both the  $\alpha$  and  $\beta$  jets ( $\beta$ -jet traces are shorter and above the  $\alpha$  traces). The panel on the right shows the same image set and traces but has been stretched to show the nucleus detail and the suggestion of source regions.

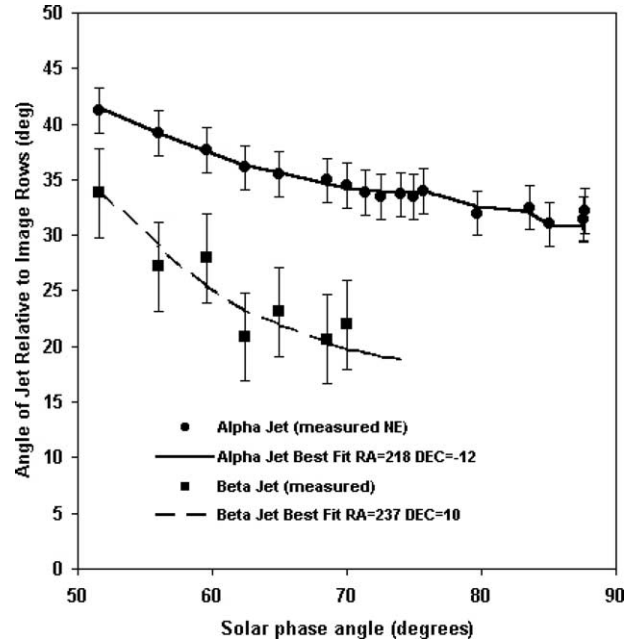


Fig. 13. Solutions for geometric orientations of the  $\alpha$  jet and  $\beta$  jet. Using angular data like that shown in Figs. 11 and 12, models for inertial orientations were computed using S/C orientation kernels and assuming the jets were fixed in direction over the periods during which they were resolved.

Using measurements of relative angles of the jet directions in the VISCCD frames, we are able to solve for the orientations of the  $\alpha$  and  $\beta$  jets in inertial space assuming that

- (1) the  $\alpha$  jet was fixed in direction, and
- (2) the change in direction of the  $\beta$  jet over the  $\sim 300$  s that it could be resolved was negligible.

Figure 13 shows a collection of measurements made from all available approach images in which the  $\alpha$  jet and  $\beta$  jets could be discerned. The angle of each jet was measured relative to the image field-of-view. These angles changed as the S/C flew past and rotated around the comet. The measurements were corrected for the small fixed image distortion inherent in the MICAS off-axis optical design using distortion polynomials of Oberst et al. (2000). The magnitude of these corrections was however negligible (standard deviation  $\sim 0.1^\circ$ ) compared to the magnitude of errors in the measured angles ( $\sim 2^\circ$  to  $5^\circ$ ). Best-fit solutions were fitted to these observations to solve for the assumed fixed inertial orientations of the  $\alpha$  and  $\beta$  jets. The disjoint pattern in the model fit (most apparent for the  $\alpha$  jet) arises from small, complex changes in S/C orientation as it performed encounter maneuvers.

Our revised solutions for the jet directions are  $RA = 218^\circ \pm 2^\circ$ ,  $DEC = -12^\circ \pm 2^\circ$  for the  $\alpha$  jet and  $RA = 237^\circ \pm 4^\circ$ ,  $DEC = 10^\circ \pm 4^\circ$  for the  $\beta$  jet, quite close to those reported earlier by Soderblom et al. (2002). At the time of the DS1 encounter, several groups observed the orientation of the sunward jet from Earth and noting that it remained fixed in orientation and lacked curvature, also con-

cluded that it must be co-aligned with the rotation axis. They all also concluded that the nucleus is in a simple rotation state. Samarasinha and Mueller (2002) reported  $RA = 221^\circ$ ,  $Dec = -7^\circ$ ; Farnham and Cochran (2002)  $214^\circ$ ,  $-5^\circ$ ; and Schleicher et al. (2003)  $214.1^\circ$ ,  $-5.7^\circ$ . All of these solutions are similar to the orientation we report for the  $\alpha$  jet at the core of the main jet. They are probably most consistent with some weighted sum of our solutions for the  $\alpha$  and  $\beta$  jets; our data provides individual solutions for the  $\alpha$  and  $\beta$  jets within 50 km or so of the nucleus, the Earth-based solutions must pertain to the composite of all the components measured out to a few thousand km from the nucleus.

Another interesting correlation arises in examining the orientation of the main jet relative to the B-plane (the plane normal to the approach vector, effectively the plane of symmetry of the encounter). By our measurements, the main jet was  $\sim 9^\circ$  out of the B-plane (toward to S/C on approach); the Earth-based values quoted above yield an average of  $\sim 14^\circ$  for this angle. A strong asymmetry was seen in the ion distributions as measured by the DS1 Plasma Experiment for Planetary Exploration or PEPE (Young et al., 2001) in which the peak in ion intensities occurred well before C/A. Young and colleagues attributed this offset to the main jet being well out of the B-plane, projecting toward the approaching S/C.

Narrow collimated jets similar to those seen at Borrelly were seen also seen at Halley and models have been constructed that involve constructive interference of gas expanding from surface sources that involve complex surface topography and/or albedo patterns (Kitamura, 1986; Korosmezey and Gombosi, 1990; Thomas and Keller, 1987; Huebner et al., 1988; Keller et al., 1994; Knollenberg et al., 1996). An alternative for collimation of the jets, involving geyser-like venting from subsurface cavities, is proposed by Yelle et al. (this issue). Earlier Sekanina (1988a, 1988b, 1991) also proposed deep vent models for jets at Encke and Tempel 2.

#### 4. Approach imaging and direction of nucleus rotation

A series of approach observations (Short Observations of Borrelly, SOB01-SOB11, 16 images each) were acquired during the month prior to encounter (Table 3). The comet was first detected in VISCCD images on August 25, 2001 at a range of  $40.3 \times 10^6$  km (Bhaskaran et al., 2002). A big uncertainty in planning the encounter was the selection of exposure times for the images. Although the general scientific view is that comet nucleus surfaces are very dark (albedos  $\sim 0.04$ ; cf. Veeder and Hanner, 1981; Hanner et al., 1987; Veeder et al., 1987; Cruikshank et al., 1985; Lamy et al., 1998; Campins et al., 1987), it was quite possible that patches or large active regions could be 10 or more times brighter. This combined with the large approach phase angle ( $\sim 88^\circ$ ) led to large uncertainties in expected brightness for the nucleus and coma. The best-observed object expected to be photometrically comparable to Borrelly's nucleus is the

C-type asteroid 253 Mathilde from the successful encounter of the NASA-Applied Physics Lab NEAR S/C. Many believe the C-type asteroids may be extinct comet nuclei and Borrelly is known to be a very mature comet with relatively subdued activity (A'Hearn et al., 1995). We adopted the photometric properties for Mathilde (albedo  $\sim 0.04$ , Veverka et al., 1997; Clark et al., 1999) as the baseline to predict VISCCD exposure times. Using the approach data we carefully monitored the increasing brightness of the coma and nucleus to insure that the final selected exposure tables were reasonable. As it turned out the Mathilde-based predictions were quite accurate.

Using the approach images we can extend the near encounter measurements of Fig. 13 back to  $-34.4$  hr, although the measured angles are less accurate for these earlier images. Figure 14 shows that the jet angles at  $-10.4$  and  $-34.4$  hr fit the model solution derived for the near encounter data well within the error bars and further illustrates that the main jet remained fixed in inertial direction for well over a full rotation period. These data are plotted as a function of time before C/A. It is clear that  $\alpha$  jet (core of the main jet) remained fixed in orientation (to within  $5^\circ$ ) for at least over a full rotation of the nucleus. The  $\beta$  jet was not discernable in these approach frames. The constancy of position of the  $\alpha$  or main jet, coupled with it being roughly normal to the long axis of the nucleus, led Soderblom et al. (2002) to conclude that it must be roughly aligned with the rotation axis of the nucleus, consistent with conclusions of the Earth-based observations (Samarasinha and Mueller, 2002; Farnham and Cochran, 2002; Schleicher et al., 2003). Also,

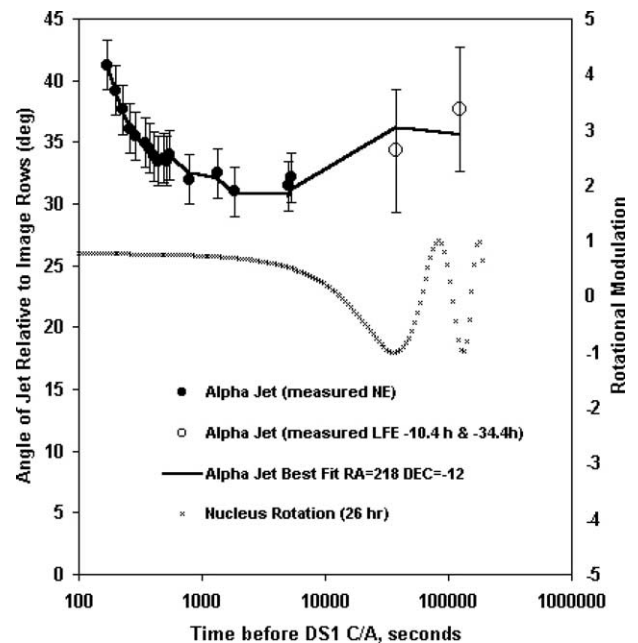


Fig. 14. The data and solutions from Fig. 13 were used to predict the apparent angles of the  $\alpha$  or main jet for images acquired 10.4 and 34.4 hr before C/A. The agreement of prediction and observation for these early images further testifies to the fixed inertial orientation of the main jet. Also shown for reference is the 26-hr rotation period (with arbitrary phase).

as noted by Soderblom et al. (2002) this main-jet-aligned rotation axis is roughly normal to the long axis of the nucleus and likely coincides with the  $c$ -axis of the nucleus. We therefore agree with Earth-based observers that the nucleus is in a stable, simple rotation state. Because the main jet is aligned with the rotation axis, disrupting torques would also be minimized.

By about a week before closest approach the SNR had increased to a sufficient level that the growing central brightness could be used to separate contributions of coma and nucleus and to distinguish the rotational modulation. The DS1 approach data set is far too sparse to independently derive a light curve. However, excellent Earth-based observations of light curve by Lamy et al. (1998) and Mueller and Samarasinha (2001, 2002) suggested nucleus aspect ratios ( $a/b$ ) and rotation periods of  $2.4 : 1$  and  $25 \pm 0.5$  hr and  $2.2 : 1$  and  $26 \pm 1$  hr, respectively. In addition, because during approach the main jet (and therefore the rotation pole) was only  $\sim 10^\circ$  out of the B-plane, we assume that the light curve amplitude was roughly equal to the aspect ratio of the nucleus. Figure 15 shows a very simple model fitted to the last six sets of approach observations (SOB06 through SOB11).

The fitted parameters in Fig. 15 are: the phase of the light curve,  $I/F_{\text{coma}}$  (the average brightness of the coma tangent to the nucleus) and  $I/F_{\text{nucleus}}$  (the average brightness of the nucleus at the approach phase angle, including the shadowed region beyond the terminator). The two  $I/F$  values, so derived, are very consistent with the near encounter data. The phase of the light curve is the most interesting feature in Fig. 15 showing that at about  $-10$  hr the light curve was near a minimum so that the nucleus was being viewed end-on. Therefore a light curve maximum would be expected at about  $-3.5$  hr (Fig. 15). During the remaining 3.5 hr up until C/A the nucleus would have rotated an additional  $\sim 50^\circ$ . Stereo images at encounter (cf. Soderblom et al., 2002; and Kirk et al. and Oberst et al., this issue) show that at near encounter, the small end of the nucleus (bottom left part in Fig. 6 views) had rotated well out of the image plane toward

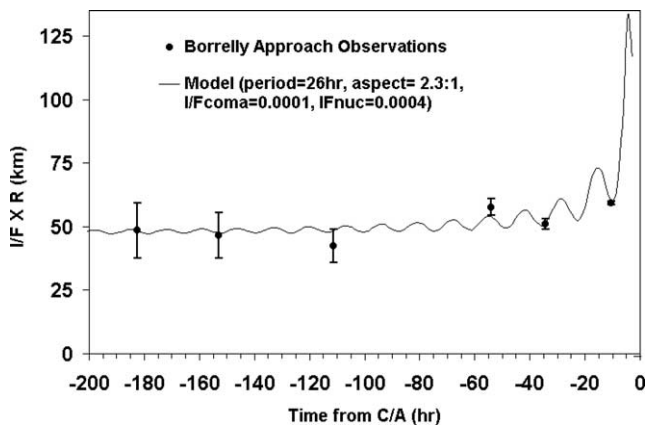


Fig. 15. Borrelly nucleus rotational light curve fitted to DS1 MICAS approach observations. Light curve period and amplitude known from Earth-based observations were used to estimate the rotational phase of the nucleus at near encounter (see text).

the S/C. This observation constrains the sense of rotation to be right-handed around the rotation pole that is aligned with the main jet. Our best estimate of the direction of the long axis at the time of encounter is roughly  $RA = 300^\circ$  and  $DEC = -10^\circ$ .

At the time of encounter, the main or  $\alpha$  jet was pointed  $\sim 35^\circ$  forward (in the prograde direction) of the sun-line and about  $3^\circ$  above the ecliptic plane. Currently there is no comet-specific IAU convention for definition of rotation poles. However, the IAU convention for planets and satellites has been provisionally extended to asteroids (Seidelmann et al., 2002) and for simple rotators is the same convention as for planets. Applying this convention, because it is above the ecliptic, we designate the axis that is co-aligned with the main jet to be the north pole of Borrelly. This configuration places the sub-solar latitude at  $\sim 55^\circ$  N at the time of encounter and at  $\sim 60^\circ$  N at perihelion. Hence the pole was in constant illumination and was also at the point of maximum average insolation. This clearly is coupled to the physical processes that drive the main jet.

## 5. The Loop

A peculiar feature that continually changed was observed to persist just beyond Borrelly's terminator in the near-encounter images. We informally refer to this feature as "the Loop" (Fig. 16). Several pieces of evidence suggest that the Loop is a feature in the coma and not on the nucleus surface. Although the phase angle changed from  $75^\circ$  to  $52^\circ$  over the  $\sim 6$  minutes interval over which the images shown in the montage were acquired, the net rotation of the nucleus was only  $\sim 1.3^\circ$ . If this feature were due to a high peak beyond the terminator it should have changed very little in appearance. Furthermore, any such small change should have been gradual and systematic. By contrast the Loop began as a small bright spot, evolved into an arc that appeared to rotate and change shape, and finally returned to the form of a small

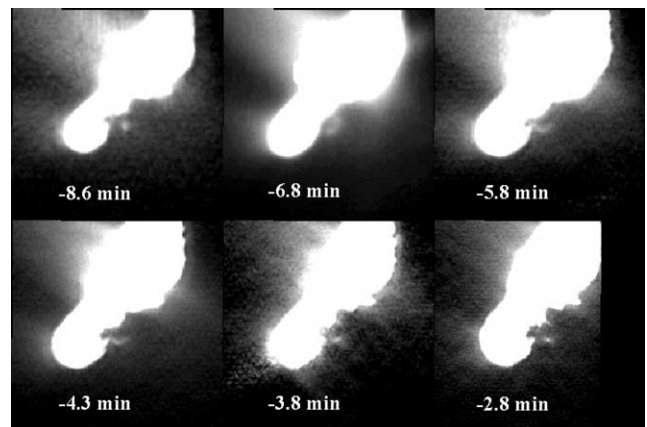


Fig. 16. Time-lapse sequence of the "Loop" feature. This enigmatic feature persisted though the near-encounter images and continually changed appearance.

bright spot. We speculate that the Loop is the signature of an active dust jet (whose source is near the terminator) that is seen in quasi-cross-section as it emerged into the sunlight above the dark terminator background. If this feature is indeed part of the coma and dust jet system it is probably less than  $\sim 1$  km above the surface. For reasonable jet velocities (of the order of 0.1 to 1 km/s) the material travels only a few seconds until it reaches the sunlight. The sequence suggests such jets to be variable on the scale of minutes.

## 6. Nucleus shape, geomorphology, and photometric properties

The Borrelly nucleus is highly variegated in styles of terrains and types of features; these new images have moved comet science into the realm of geology (cf. Britt et al., this issue). The nucleus is fundamentally divisible into two terrain types: slightly brighter smooth rolling plains (that occupy the central basin from which the main jet emanates and the small sunward end from which the fan jet originates) and darker, rougher mottled terrain that appears inactive, perhaps as a lag surface. Quasi-circular depressions are visible at the limit of resolution, but it is difficult to unambiguously identify any of impact origin. Certainly no fresh impact craters down to  $\sim 200$ -m diameter are evident testifying to a young and active surface. Images of any minor satellite or asteroid, so far acquired of this quality and scale, show ample impact craters. Quasi-circular depressions are most abundant in the Mottled Terrain, but these have roughly similar diameters indicating that they may be the product of surface desiccation.

The surface of Borrelly's nucleus is covered with extremely dark material, the average normal albedo of the surface is only  $0.03 \pm 0.01$ . This surface is among the darkest observed in the solar system (cf. Buratti et al., this issue). The assumption (Soderblom et al., 2002) that the photometric behavior of the nucleus would be similar to that of the C-type asteroid 253 Mathilde (Veverka et al., 1997; Clark et al., 1999) was born out. Borrelly's geometric albedo is comparable to the darkest C-type asteroids and the low-albedo side of Iapetus (Tedesco et al., 1989; Ockert et al., 1987; Buratti and Mosher, 1995).

An arguable question is whether or not any of the very dark spots represent real albedo variations on the nucleus or whether they are simply due to shadows. Nelson et al. and Kirk et al. (this issue) examine this question and conclude that at least some of the dark spots are dark albedo patches while others could be depressions or pits. The conclusion is that in addition to topographic roughness, the nucleus may well exhibit a wide range of normal albedo from as low as  $\sim 0.01$  and to as high as  $\sim 0.04$ .

## 7. Conclusions and summary

Observations of Comet 19P/Borrelly with the Miniature Integrated Camera and Spectrometer aboard Deep Space 1

have yielded important new data for both the understanding and planning of future exploration of comets.

- Borrelly's near nucleus coma is dominated by two main jets: a sun-pointed fan jet and a collimated main jet both of which remained fixed in position throughout the encounter.
- We conclude that the main jet is aligned with the rotation axis and remains fixed in orientation; while the fan jet tracks the Sun as the nucleus rotates generating a moving fan at the sub-solar point.
- Modulation in the intensity of the fan jet arises as the sub-solar point moves across the nucleus across areas more or less volatile rich. The small end, sun-pointed at encounter, was evidently far less prolific than when the opposite hemisphere faced the Sun.
- Our revised solutions for the jet directions are  $RA = 218^\circ \pm 2^\circ$ ,  $DEC = -12^\circ \pm 2^\circ$  for the  $\alpha$  jet which is at the core of the main jet and  $RA = 237^\circ \pm 4^\circ$ ,  $DEC = 10^\circ \pm 4^\circ$  for the  $\beta$  jet which is the principal subsidiary jet.
- Earth-based observations for the sunward jet at the time of the DS1 encounter ranged from  $RA \sim 214^\circ$  to  $221^\circ$  and  $DEC \sim -5^\circ$  to  $-7^\circ$ . We believe these probably represent weighted sum of our solutions for the  $\alpha$  and  $\beta$  jets; our data provides individual solutions for the  $\alpha$  and  $\beta$  jets within 50 km or so of the nucleus, the Earth-based solutions pertain to the composite of all the components measured out to a few thousand km from the nucleus.
- From our measurements, the main jet was  $\sim 9^\circ$  out of the B-plane (toward to S/C on approach); Earth-based values yield an average of  $\sim 14^\circ$  for this angle. This is consistent with a strong asymmetry was seen in the ion distributions as measured by the DS1 Plasma Experiment for Planetary Exploration or PEPE in which the peak in ion intensities occurred well before C/A.
- The inferred rotation axis (aligned with the main jet) is roughly normal to the long axis of the nucleus and likely coincides with the  $c$ -axis of the nucleus. We therefore agree with Earth-based observers that the nucleus is in a stable, simple rotation state. Because the main jet is aligned with the rotation axis, disrupting torques would also be minimized.
- Lacking a comet-specific IAU convention for definition of rotation poles but applying the convention provisionally adopted for asteroids, because the estimate direction of this jet or pole is  $3^\circ$  ecliptic latitude, we designate the axis that is co-aligned with the main jet to be the north pole of Borrelly. This configuration places the sub-solar latitude at  $\sim 55^\circ$  N at the time of encounter and at  $\sim 60^\circ$  N at perihelion. Hence the pole was in constant illumination and was also at the point of maximum average insolation. This clearly is coupled to the physical processes that drive the main jet.
- The direction of rotation of the nucleus is right-handed around the north pole.

## Acknowledgments

This research was completed under NASA funding from the New Millennium Deep Space 1 Project conducted by the Jet Propulsion Laboratory of the California Institute of Technology. Careful reviews by T. Farnham, K. Herkenhoff, D. Schleicher, and T. Stone were invaluable.

## References

- A'Hearn, M.F., Millis, R.L., Schleicher, D.G., Osip, D.J., Birch, P.V., 1995. The ensemble properties of comets: results from narrowband photometry of 85 comets, 1976–1992. *Icarus* 118, 223–270.
- Beauchamp, P.M., Brown, R.H., Bruce, C.F., Chen, G.-S., Crisp, M.P., Fraschetti, G.A., Krabach, T.N., Petrick, S.W., Rodgers, D.H., Rodriguez, J., Soll, S.L., Vaughan, A.H., Soderblom, L.A., Sandel, B.R., Yelle, R.V., 1994. Pluto integrated camera spectrometer (PICS) instrument. In: *Proc SPIE*, Vol. 2214. pp. 269–277.
- Bhaskaran, S., Riedel, J.E., Kennedy, B., Wang, T.C., 2002. Navigation of the Deep Space 1 Spacecraft at Borrelly. In: *AIAA/AAS Astrodynamics Specialist Conference and Exhibit*, Monterey, CA. AIAA paper 2002-4815.
- Buratti, B.J., Mosher, J.A., 1995. The dark side of Iapetus: additional evidence for an exogenous origin. *Icarus* 115, 219–227.
- Campins, H., A'Hearn, M.F., McFadden, L.A., 1987. The bare nucleus of Comet Neujmin 1. *Astrophys. J.* 316, 847–857.
- Clark, B., Veverka, J., Helfenstein, P., Thomas, P.C., Bell III, J.F., Harch, A., Robinson, M.S., Murchie, S.L., McFadden, L.A., Chapman, C.R., 1999. NEAR photometry of Asteroid 253 Mathilde. *Icarus* 140, 53–65.
- Cruikshank, D.P., Hartmann, W.K., Tholen, D.J., 1985. Colour, albedo and nucleus size of Halley's comet. *Nature* 315, 122–124.
- Farnham, T.L., Cochran, A.L., 2002. A McDonald observatory study of Comet 19P/Borrelly: placing the Deep Space 1 observations into a broader context. *Icarus* 160, 398–418.
- Hanner, M.S., Newburn, R.L., Spinrad, H., Veeder, G.J., 1987. Comet Sugano-Saigusa-Fujikawa (1983V)—a small, puzzling comet. *Astron. J.* 94, 1081–1087.
- Huebner, W.F., Boice, D.C., Reitsema, H.J., Delamere, W.A., Whipple, F.L., 1988. A model for intensity profiles of dust jets near the nucleus of Comet Halley. *Icarus* 76, 78–88.
- International Astronomical Union Minor Planets Circular 31664, 1998.
- Keller, H.U., Delamere, W.A., Reitsema, H.J., Huebner, W.F., Schmidt, H.U., 1987. Comet P/Halley's nucleus and its activity. *Astron. Astrophys.* 187, 807–823.
- Keller, H.U., Knollenberg, J., Markiewicz, W.J., 1994. Collimation of cometary dust jets and filaments. *Planet. Space Sci.* 42, 367–382.
- Kitamura, Y., 1986. Axisymmetric dusty gas jet in the inner coma of a comet. *Icarus* 66, 241–257.
- Knollenberg, J., Kuhrt, E., Keller, H.U., 1996. Interpretation of HMC images by a combined thermal and gasdynamic model. *Earth Moon Planets* 72, 103–112.
- Korosmezey, A., Gombosi, T.I., 1990. A time-dependent dusty gas dynamic model of axisymmetric cometary jets. *Icarus* 84, 118–153.
- Lamy, P.L., Toth, I., Weaver, H.A., 1998. Hubble Space Telescope observations of the nucleus and inner coma of Comet 19P/1904 Y2 (Borrelly). *Astron. Astrophys.* 337, 945–954.
- Lee, M., Weidner, R.J., Soderblom, L.A., 2002. Deep space one mission and observation of Comet Borrelly. In: *45th IEEE International Midwest Symposium on Circuits and System (MWSCAS 2002)*.
- Mueller, B., Samarasinha, N., 2001. Lightcurve observations of 19P/Borrelly. *Bull. Amer. Astron. Soc.* 33, 1090.
- Mueller, B.E.A., Samarasinha, N.H., 2002. Visible lightcurve observations of Comet 19P/Borrelly. *Earth Moon Planets* 90, 463–471.
- Oberst, J., Brinkmann, B., Giese, B., 2000. Geometric calibration of the MICAS CCD sensor on the DS1 (Deep Space One) spacecraft: laboratory vs. inflight data analysis. In: *ISPRS 3rd, Amsterdam. #221 [CD-ROM]*.
- Ockert, M.E., Cuzzi, J.N., Porco, C.C., Johnson, T.V., 1987. Uranian ring photometry—results from Voyager 2. *J. Geophys. Res.* 92, 14969–14978.
- Rayman, M.D., 2002. The Deep Space 1 extended mission: challenges in preparing for an encounter with Comet Borrelly. *Acta Astronaut.* 51, 507.
- Rayman, M.D., Varghese, P., 2001. The Deep Space 1 extended mission. *Acta Astronaut.* 48, 693.
- Rayman, M.D., Varghese, P., Lehman, D.H., Livesay, L.L., 2001. Results from the Deep Space 1 technology validation mission. *Acta Astronaut.* 47, 475.
- Samarasinha, N.H., Mueller, B.E.A., 2002. Spin axis direction of Comet 19P/Borrelly based on observations from 2000 and 2001. *Earth Moon Planets* 90, 473–482.
- Schleicher, D.G., Woodney, L.M., Millis, R.L., 2003. Comet 19P/Borrelly at multiple apparitions: seasonal variations in gas production and dust morphology. *Icarus* 162, 415–442.
- Seidelmann, P.K., Abalakin, V.K., Bursa, M., Davies, M.E., De Bergh, C., Lieske, J.H., Oberst, J., Simon, J.L., Standish, E.M., Stooke, P., Thomas, P.C., 2002. Report of the IAU/IAG working group on cartographic coordinates and rotational elements of the planets and satellites: 2000. *Celest. Mech. Dynam. Astron.* 82, 83–110.
- Sekanina, Z., 1988a. Outgassing asymmetry of periodic Comet Encke I. Apparitions 1924–1984. *Astron. J.* 95, 911–924.
- Sekanina, Z., 1988b. Outgassing asymmetry of periodic Comet Encke II. Apparitions 1868–1918 and a study of the nucleus evolution. *Astron. J.* 96, 1455–1475.
- Sekanina, Z., 1991. Comprehensive model for the nucleus of periodic Comet Tempel 2 and its activity. *Astron. J.* 102, 350–388.
- Soderblom, L.A., Beauchamp, P.M., Chen, G.-S., Elliott, S.T., Fraschetti, G.A., Lee, M., Pain, B., Petrick, S.W., Ringold, P.G., Rodgers, D.H., Sandel, B.R., Soll, S.L., Thomas, D.A., Wang, D., 2000. Miniature Integrated Camera Spectrometer (MICAS) technology validation report. In: *Extended Abstracts and Fact Sheets: Deep Space 1 Technologies, Deep Space 1 Technology Validation Symposium*, February 8–9, 2000, Pasadena CA.
- Soderblom, L.A., Becker, T.L., Bennett, G., Boice, D.C., Britt, D.T., Brown, R.H., Buratti, B.J., Isbell, C., Giese, B., Hare, T., Hicks, M.D., Howington-Kraus, E., Kirk, R.L., Lee, M., Nelson, R.M., Oberst, J., Owen, T.C., Sandel, B.R., Rayman, M.D., Stern, S.A., Thomas, N., Yelle, R.V., 2002. Observations of Comet 19P/Borrelly by the miniature integrated camera and spectrometer aboard Deep Space 1. *Science* 296, 1087–1091.
- Tedesco, E., Williams, J.G., Matson, D.L., Veeder, G.J., Gradie, J.C., Lebofsky, L.A., 1989. A three-parameter asteroid taxonomy. *Astron. J.* 97, 580–606.
- Thomas, N., Keller, H.U., 1987. Fine dust structures in the emission of Comet P/Halley observed by the Halley multicolour camera on board Giotto. *Astron. Astrophys.* 187, 843–846.
- Veeder, G.J., Hanner, M.S., 1981. Infrared photometry of Comets Bowell and P/Stephan-Oterma. *Icarus* 47, 381–387.
- Veeder, G.J., Hanner, M.S., Tholen, D.J., 1987. The nucleus of Comet P/Arend-Rigaux. *Astron. J.* 94, 169–173.
- Veverka, J., Thomas, P., Harch, A., Clark, B., Bell III, J.F., Carcich, B., Joseph, J., Chapman, C., Merline, W., Robinson, M., Malin, M., McFadden, L.A., Murchie, S., Hawkins III, S.E., Farquhar, R., Izenberg, N., Cheng, A., 1997. NEAR's Flyby of 253 Mathilde: images of a C asteroid. *Science* 278, 2109.
- Weaver, H.A., Stern, S.A., Parker, J.W., 2003. HST/STIS Observations of Comet 19P/Borrelly during the Deep Space 1 Encounter. *Astron. J.* 126, 444–451.
- Young, D.T., Cray, F.J., Nordholt, J.E., Hanley, J.J., Burch, J.L., McComas, D.J., Goldstein, R., Boice, D., Wiens, R.C., Lawrence, D.R., Eviatar, A., Sauer, K., Meier, R., 2001. Solar wind interactions with the coma of Comet 19P/Borrelly. In: *American Astronomical Society, DPS Meeting 3rd*. 26.03.